INTERNATIONAL JOURNAL FOR NUMERICAL METHODS IN FLUIDS
Int. J. Numer. Meth. Fluids 2002; **38**:207–226 (DOI: 10.1002/fld.208)

Transition from vortex to wall driven turbulence production in the Taylor–Couette system with a rotating inner cylinder

W. M. J. Batten, N. W. Bressloff and S. R. Turnock*,†

School of Engineering Sciences, University of Southampton, Southampton, S017 1BJ, U.K.

SUMMARY

Axisymmetrically stable turbulent Taylor vortices between two concentric cylinders are studied with respect to the transition from vortex to wall driven turbulent production. The outer cylinder is stationary and the inner cylinder rotates. A low Reynolds number turbulence model using the k-ω formulation, facilitates an analysis of the velocity gradients in the Taylor–Couette flow. For a fixed inner radius, three radius ratios 0.734, 0.941 and 0.985 are employed to identify the Reynolds number range at which this transition occurs. At relatively low Reynolds numbers, turbulent production is shown to be dominated by the outflowing boundary of the Taylor vortex. As the Reynolds number increases, shear driven turbulence (due to the rotating cylinder) becomes the dominating factor. For relatively small gaps turbulent flow is shown to occur at Taylor numbers lower than previously reported. Copyright © 2002 John Wiley & Sons, Ltd.

KEY WORDS: Taylor–Couette flow; CFD; low Reynolds number turbulence; k-ω

1. INTRODUCTION

The flow between a rotating inner cylinder and a fixed outer cylinder is of interest in several engineering applications, such as motors, filters, pumps and journal bearings. The motivation for this work stemmed from the development of a novel underwater-integrated electrical thruster unit [1–3]. A significant source of power loss in the electrical thruster arises from the frictional resistance that occurs between two such cylinders.

This flow has been studied since Taylor [4] reported the formation of an array of alternating laminar toroidal vortices at a particular speed dependent upon the geometry of the problem. The Taylor number is defined as

$$Ta = Re^2 \frac{d}{R_1} \tag{1}$$

*Correspondence to: S. R. Turnock, School of Engineering Sciences, University of Southampton, Southampton, S017 1BJ, U.K.
†E-mail: s.r.turnock@soton.ac.uk

Received July 2000
Revised March 2001

Where Re is the Reynolds number based on gap width,

$$Re = \frac{Ud}{v} \tag{2}$$

d is the gap width, R_1 is the inner radius, U is the speed of the inner cylinder and v is the kinematic viscosity. The Taylor number at which these vortices first appear is known as the critical Taylor number, Ta_c. As the Taylor number is further increased, the flow changes through various wavy and chaotic states to turbulent flow. Koschmieder [5] stated that when $Ta \approx 1000 Ta_c$ order emerges from chaotic flow and the flow is turbulent with axisymmetric stable uniform vortices. This corresponded to a $Re = 4.16 \times 10^3$ with a radius ratio, $\eta = [(R_1)/(R_2)] = 0.896$, where the outer radius $R_2 = R_1 + d$.

The current paper analyses turbulent Taylor vortices in the Reynolds number range $5 \times 10^3 < Re < 5 \times 10^4$ for three different radius ratios $\eta = 0.7246$ [6], $\eta = 0.9412$ [7] and $\eta = 0.9846$ [1]. Based on an inner radius of 128 mm, which is approximately equal to that in References [7] and [1], these values of η correspond to a gap width of 48.64 mm, 8.00 mm and 2.00 mm, respectively. Hence forth, the analysis will refer to the 48 mm, 8 mm and 2 mm test cases. This paper demonstrates that stable axisymmetric turbulent Taylor vortices occur for a relatively small gap (the 2 mm case) at Taylor numbers significantly lower than the value of $1000 T_c$ suggested by Koschmieder. Also, by analysing components in the turbulent production terms of the k-ω model [8] a transition is identified at all three radius ratios as the flow becomes more like a wall bounded shear flow.

Experimental evidence for this transition exists in the detailed torque measurements of Taylor–Couette flow from which various semi-empirical equations have been derived. The two most commonly used are due to Wendt given in Reference [6] and Bilgen and Boulos [9]. Both of these sets of equations are based on a power law for Reynolds number, $Re \approx 10^4$.

Wendt's empirical equations are

$$G = \begin{cases} 1.45 \left(\dfrac{\eta^{3/2}}{(1-\eta)^{7/4}} \right) Re^{1.5} & \text{for } 4 \times 10^2 < Re < 1 \times 10^4 \\ 0.23 \left(\dfrac{\eta^{3/2}}{(1-\eta)^{7/4}} \right) Re^{1.7} & \text{for } 1 \times 10^4 < Re < 1 \times 10^5 \end{cases} \tag{3}$$

where, $G = M/\rho v^2 L$, M is the moment, L is the length and ρ is the density.

Bilgen and Boulos' empirical equations are

$$C_M = \begin{cases} 1.03 \left(\dfrac{d}{R_1} \right)^{0.3} Re^{-0.5} & \text{for } 5 \times 10^2 < Re < 1 \times 10^4 \\ 0.065 \left(\dfrac{d}{R_1} \right)^{0.3} Re^{-0.2} & \text{for } Re > 1 \times 10^4 \end{cases} \tag{4}$$

where, $C_M = M/1/2\pi\rho U^2 R_1^2 L$.

Wendt's equations can also be expressed in terms of C_M:

$$C_M = \begin{cases} 0.923 \left(\dfrac{dR_2}{R_1^2}\right)^{0.25} Re^{-0.5} & \text{for } 4 \times 10^2 < Re < 1 \times 10^4 \\ 0.146 \left(\dfrac{dR_2}{R_1^2}\right)^{0.25} Re^{-0.2} & \text{for } 1 \times 10^4 < Re > 1 \times 10^5 \end{cases} \tag{5}$$

Bilgen *et al.*'s equations are based on the authors' own experimental data and other data available in Wendt [6], Taylor [10] and Donnelly and Simon [11]. They collected data in the Reynolds numbers range $10 < Re < 1 \times 10^6$ and radius ratios, $\eta = [(R_1)/(R_2)]$, ranging from $0.5 < \eta < 0.988$. From this, they deduced four semi-empirical expressions for the skin friction, C_M. The two equations that are relevant to this paper are given in Equation (4), stated to an accuracy of ± 8.35 per cent.

Although numerous studies of Taylor–Couette flow at low Reynolds numbers have been carried out (see, for example References [12] and [13]), most are concerned with the formation of laminar vortices and the various wavy states formed as the flow becomes chaotic. There have been a few experimental studies at higher Reynolds numbers; notably visualization work by Burkhalter and Koschmieder [14], who made detailed vortex wavelength measurements for several cylinder combinations and Townsend [15], who conducted a series of turbulent hot-wire probe experiments.

More recently, turbulent Taylor vortices have been studied at high Reynolds numbers using Laser Doppler Velocimetry [16]. This study used refractive index matching techniques and showed that Taylor Vortices are still present at $Ta = 2.107 \times 10^9$ ($Re = 73440$). Lathrop *et al.* [6] studied the turbulent flow between concentric cylinders for Reynolds numbers between $800 < Re < 1.23 \times 10^6$ with a radius ratio of $\eta = 0.7246$. While these experiments reveal no such Reynolds number change in torque based on a fixed power law akin to that of Bilgen and Boulos [9], they did show a hysteretic free transition at a Reynolds number of 1.3×10^4. Above this Reynolds number the experiments suggest that the nature of the flow behaviour is more like that of open-flow systems such as those found in pipes or ducts.

Turbulent Taylor vortex flow in a centrifugal rotor was studied both experimentally and computationally by Wild *et al.* [7]. Two radius ratios were considered, $\eta = 0.941$ and 0.974 at Reynolds numbers in the range, $1.5 \times 10^4 < Re < 4 \times 10^4$. For their test cases the experimental results were in relatively good agreement with the semi-empirical expressions of Wendt and Bilgen *et al.* The computational study employed the standard k-ε model [17] which over-predicted their experimental results by 10 per cent or higher. Computations were also performed using other turbulence models with wall functions; the Renormalization Group (RNG) model [18] was within 2 per cent of the standard k-ε model and the Reynolds Stress Equation model (RSM) [19] was 40 per cent higher than the k-ε model. The RNG model without a wall function was also 40 per cent higher than the k-ε model.

These results are surprising as the RNG and RSM models are generally thought to be more suitable for flows with curvature and rotation than the standard k-ε model [8]. This may be due to the fact that the turbulence models are more sensitive to the chosen coefficients and that these models have not been tuned for this problem. In the present work, as the gaps are small and the Reynolds number range is relatively low, adjacent grid points to the walls lie

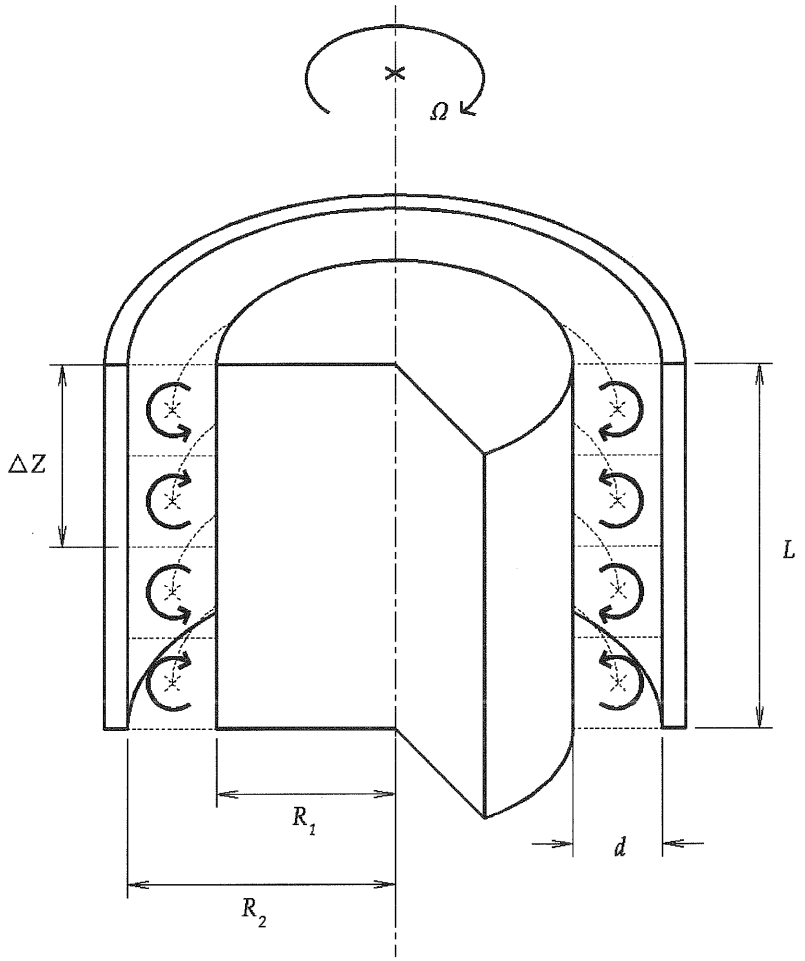

Figure 1. Schematic section of the geometry.

within the sublayer leading to large inaccuracies with the standard k-ε model. To overcome this problem the Wilcox low Reynolds number k-ω model [8] is used.

2. COMPUTATIONAL METHOD

The problem considered is that of steady state turbulent Taylor vortices between a rotating inner cylinder and a stationary outer cylinder, as shown schematically in Figure 1. The flow is solely induced by the relative motion of the inner cylinder. Assuming that the flow can be modelled using the Reynolds-averaged Navier–Stokes equations and that the vortices are uniform and not travelling in waves around the cylinders, the domain can then be simplified as a 2-D axial slice with a pair of periodic boundaries. Presuming the Taylor vortices are

Table I. Critical laminar Taylor numbers and wavelengths.

Case	η	Ta_c	$\triangle Z_T$
2 mm	0.9846	1721	5.01 mm
8 mm	0.9412	1760	20.1 mm
48 mm	0.7246	1981	117.25 mm

symmetrical, a mirror boundary is placed at either end of the vortex. The vortex sizes are constrained by the length of the domain, which is defined as follows.

Chandrasekhar showed in Reference [20] by using linear theory that instability between two cylinders with the inner cylinder rotating is governed by

$$Ta = \frac{2}{1+\eta} \cdot \frac{(\pi^2 + a^2)^3}{1 - 16a\pi^2 \cosh^2(a/2)((\pi^2 + a^2)^2(\sinh a + a))} \tag{6}$$

where a is the Taylor vortex wave number.

This equation has a minimum, which refers to the critical Taylor number, Ta_c at which the vortices are formed. At this critical number, there is an associated wave number a_c. This wave number is given by $\lambda = 2\pi/a$, where λ is a non-dimensional size of a pair of Taylor vortices, $\lambda = \Delta Z/d$. ΔZ signifies the length of a pair of vortices and d is the gap width.

The turbulent Taylor vortex cell length is highly dependent upon the start-up conditions. As Burkhalter and Koschmieder reported in Reference [14], the wavelength varied from 20 per cent larger than the critical value during rapid accelerations to 70 per cent larger during quasi-steady accelerations (accelerations much less than the relaxation time, d^2/v). Many engineering applications employ rapid accelerations so a wavelength for the Taylor vortices was taken to be $1.25 \times \lambda$. Using Equation (6) and taking the turbulent vortex length to be $\Delta Z_T = 1.25 \times \Delta Z$, the critical Taylor numbers and turbulent wave lengths for the three test cases examined are given in Table I.

A uniform cell distribution in the axial direction was used as the axial velocity tended to vary uniformly along the length of one cell. However, a non-uniform expanding and then contracting grid was used in the radial direction. This was set up to place sufficient cells in the laminar sublayer, defined by, [6]

$$\frac{\delta_1}{R_1} = 6.32 \cdot (\eta^{-1} - 1)^{2/3} \cdot Re^{-2/3} \tag{7}$$

$$\frac{\delta_2}{R_2} = 8.16 \cdot (\eta^{-1} - 1)^{2/3} \cdot Re^{-2/3} \tag{8}$$

where δ_1 is the laminar sublayer thickness on the inner cylinder and δ_2 is the corresponding thickness on the outer cylinder. Applying Equations (7) and (8) to the present cases the widths of the turbulent cores are presented in Table II. The sublayer region comprises a significant proportion of the gap especially for the 2 mm case.

The Taylor–Couette problem was simulated using a commercial RANS flow solver [21]. This is a structured multi-block finite volume code. Turbulence was modelled using the low

Table II. Comparison of the percentage of turbulent core.

Re	2 mm	8 mm	48 mm
5×10^3	80	87	92
1×10^4	87	92	95
5×10^4	96	97	98

Reynolds number Wilcox Model as described in the following section. The QUICK differencing scheme was used in the SimpleC pressure correction algorithm and Algebraic Multi-grid was used to accelerate convergence.

To ensure that the solution had converged, residuals were analysed to confirm that all components had reduced to a steady state and that there were no oscillatory motions in the final solution. The residuals were normalized with respect to the absolute mean value. The normalized axial and radial velocities residuals were less than 10^{-3}. All other residuals converged to less than 10^{-6}.

The 8 mm case was used to test for a grid independent solution at $Re=8\times10^3$ and $Re=1.6\times10^4$. The inflow and outflow profiles were aligned with the vortex end cells in the 32×32 case. The velocity profile plots are shown in Figures 2 and 3, and the shear stress is presented in Tables III and IV. The results show good alignment of the mean profiles, with small changes in the inflow and outflow profiles with the shear stress coefficient, C_M. Therefore, the 64×64 grid was used for the remainder of the test cases to save computation cost as increasing the grid density had little improvement upon the accuracy.

2.1. *Low Reynolds number turbulent Wilcox model*

Turbulence has been modelled using the low Reynolds number Wilcox Model [8]. Since this model avoids the use of wall functions, it allows modelling close to the wall and provides more accurate modelling of turbulent production due to the Taylor vortex formation. The transport equations for the turbulent kinetic energy, k, and the turbulent frequency, ω are given by [21]

$$\frac{\partial}{\partial t}\rho k+\nabla\bullet(\rho k\mathbf{U})=\nabla\bullet\left[\left(\mu+\frac{\mu_{\mathrm{T}}}{\sigma_k}\right)\nabla k\right]+P-\rho\omega k \tag{9}$$

and

$$\frac{\partial}{\partial t}\rho\omega+\nabla\bullet(\rho\omega\mathbf{U})=\nabla\bullet\left[\left(\mu+\frac{\mu_{\mathrm{T}}}{\sigma_k}\right)\nabla k\right]+C_1\frac{\omega}{k}P-C_2\rho\omega^2 \tag{10}$$

where μ is the dynamic viscosity and the constants $C_1=0.5111$, $C_2=0.8333$ and $\sigma_k=2$ (Prandtl number). The turbulent production term, P is expressed as

$$P=\mu_{\mathrm{T}}\nabla\mathbf{U}\bullet(\nabla\mathbf{U}+(\nabla\mathbf{U})^T) \tag{11}$$

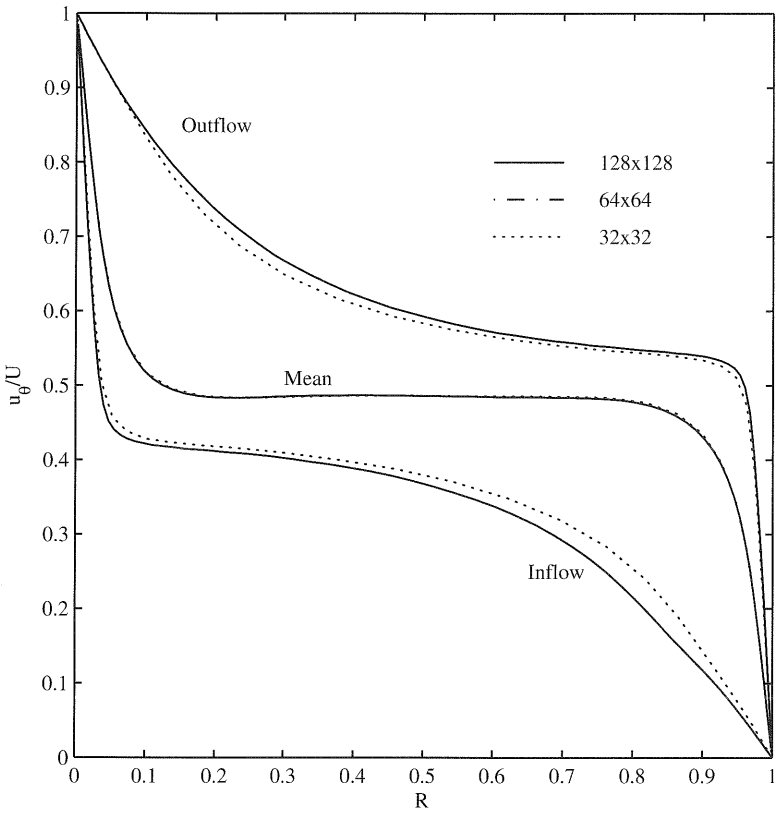

Figure 2. Profile plot for the 8 mm case, $Re = 8 \times 10^3$.

The turbulent viscosity is defined by

$$\mu_T = C_\mu f_\mu \rho \frac{k}{\omega} \tag{12}$$

taking $C_\mu = 0.09$ and the damping function f_μ given by

$$f_\mu = \exp\left[\frac{-3.4}{(1 + R_T/50)^2}\right] \tag{13}$$

with a local turbulent Reynolds number

$$R_T = \frac{\rho k}{\mu \omega} \tag{14}$$

When analysing the turbulent energy in the Taylor–Couette system the turbulent production derivatives in polar coordinates are: $(\partial u_r/\partial x)^2$, $(\partial u_\theta/\partial x)^2$, $(\partial u_x/\partial r)^2$, $(\partial u_\theta/\partial r)^2$, $2(\partial u_x/\partial x)^2$, $2(\partial u_r/\partial r)^2$, $(\partial u_x/\partial r)(\partial u_r/\partial x)$, $(\partial u_r/\partial x)(\partial u_x/\partial r)$ and the turbulent dissipation term is $\rho\omega k$, where the components u_r, u_θ, u_x, r and x are the radial, azimuthal and axial velocities and the radial and axial distances, respectively.

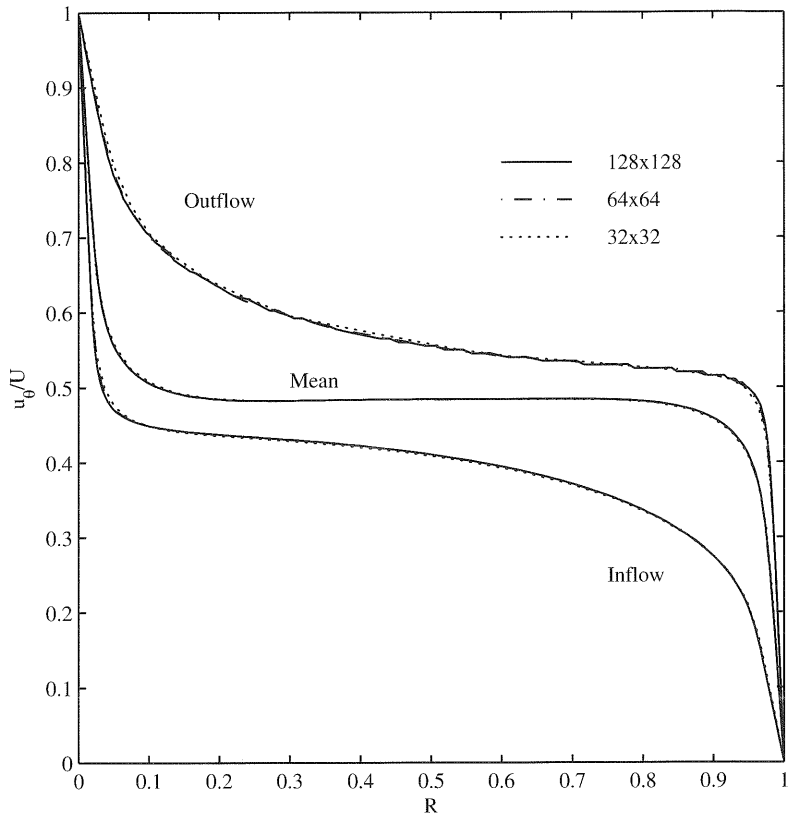

Figure 3. Profile plot for the 8 mm case, $Re = 1.6 \times 10^4$.

Table III. C_M for the 8 mm case, $Re = 8 \times 10^3$.

Grid dimensions	CV	Shear stress
16×16	256	5.30e−03
32×32	1024	4.79e−03
64×64	4096	4.82e−03
128×128	16384	4.83e−03

Table IV. C_M for the 8 mm case, $Re = 1.6 \times 10^4$.

Grid dimensions	CV	Shear stress
16×16	256	4.26e−03
32×32	1024	3.87e−03
64×64	4096	3.70e−03
128×128	16384	3.73e−03

The low Reynolds number effects at the wall are accounted for by applying the exact solution to the ω equation in the viscous sublayer,

$$\omega \sim \frac{6\mu}{\rho C_2 y^2} \quad \text{for } y^+ < 2.5 \tag{15}$$

where y is the distance from the wall, $y^+ = [(y\sqrt{\rho\tau_w})/\mu]$ and τ_w is the shear stress at the wall. To minimize the numerical error of the integration through the sublayer and to ensure y^+ independent results, the first 7 to 10 grid points from the walls were positioned between $0 < y^+ < 2.5$ as advised in Reference [8].

3. RESULTS

The results are validated against the empirical equations given by Bilgen *et al.* and are given in Table V. For the 2 mm test case the numerical simulations over predict the empirical relationship by around 20 per cent. The 8 mm case predicted the skin friction almost within Bilgen *et al.*'s margin of error, with the exception of the low speed case, $Re = 5000$, where the CFD analysis over estimated by around 50 per cent. This was possibly due to the very low turbulent production. The results for the 48 mm test case were inconsistent due to numerical problems, hence three results are presented for the 48 mm case.

The components of the turbulent Taylor vortex are compared in a series of non-dimensional profile plots either side of the transition for all three test cases. The velocity components, kinetic energy and the dissipation and production terms have been non-dimensionalized by the speed of the inner cylinder, U, the square of the shear stress velocity, $u_\tau = \sqrt{\tau_w/\rho}$ and a parameter $[(\nu)/(\rho u_\tau^4)]$, respectively. These terms are plotted against a non-dimensional radius, $R = [(r - R_1)/d]$ and the length $L = [l/d]$.

The associated Reynolds numbers and figure numbers describing conditions before and after transition for all three test cases are presented in Table VI.

Table V. Comparison of C_M values between the Empirical equations of Bilgen and Boulos [9] and the current CFD calculations.

Test case	*Re*	Empirical	CFD	%
2 mm	5000	0.0042	0.0045	8
2 mm	8000	0.0033	0.0039	15
2 mm	10000	0.0030	0.0036	19
2 mm	20000	0.0026	0.0031	16
8 mm	5000	0.0063	0.013	52
8 mm	8000	0.0050	0.0048	−4
8 mm	16000	0.0041	0.0037	−9
8 mm	20000	0.0039	0.0042	7
48 mm	8000	0.0084	0.0067	−25
Square 48 mm	8000	0.0084	0.0084	1
Square 48 mm	20000	0.0065	0.0046	41

Table VI. List of Re, Ta/Ta_c and figure numbers for the test cases before and after transition.

Test case	Before transition	After transition
2 mm	$Re = 5.00 \times 10^3$ $Ta/Ta_c = 224$ see Figure 7	$Re = 8.00 \times 10^3$ $Ta/Ta_c = 573$ see Figure 8
8 mm	$Re = 8.00 \times 10^3$ $Ta/Ta_c = 2140$ see Figure 9	$Re = 1.60 \times 10^4$ $Ta/Ta_c = 8550$ see Figure 10
48 mm	$Re = 8.00 \times 10^3$ $Ta/Ta_c = 8900$ see Figures 4 and 6	$Re = 2.00 \times 10^4$ $Ta/Ta_c = 55600$ see Figure 5

At $Re = 2 \times 10^4$ for the 48 mm case the numeric model was unsteady. Several attempts to force a converged solution were tried by altering the grid distribution, grid densities and initial conditions. The only method of achieving a converged solution was by altering the aspect ratio of the vortex cell size. When the cell aspect ratio was reduced to unity, $\Delta Z_T = 96$ mm, the solution converged either side of the transition but with two vortices. This is shown in Figures 4 and 5. The converged single cell case with an aspect ratio of 1.25 is also presented in Figure 6 for comparison.

The axial and radial velocity components, u_x and u_r, for both the 2 mm and 8 mm case are similar (Figures 7–10). The velocity components are larger for the 8 mm case than for the 2 mm case; this is further demonstrated in Figures 6(a) and (b) for the 48 mm case where the maximum non-dimensionalized velocity has doubled. The azimuthal velocity components, u_θ, are also consistent across Figures 4–10(c) with higher axial gradients than radial gradients before the transition.

The turbulent kinetic energy plots, k (Figures 7(g) and 9(g)) have maximum peaks in the radial plane, at the outflow edge of the vortex. After the transition, Figures 8(g) and 10(g) have maximum peaks in the axial direction, along the edge of the inner cylinder. This is also demonstrated in Figures 4(g) and 5(g) with two vortices.

The two most significant contributions, by a factor of approximately 1000, to the production of turbulent kinetic energy are due to the azimuthal velocity gradients in the radial direction $\mu_T(du_\theta/du_r)^2$ (Figures 4–10(d)) and in the axial direction $\mu_T(du_\theta/du_x)^2$ (Figures 4–10(e)). The test cases show relatively larger peaks in the radial production, vortex boundaries, than the axial production, wall boundaries, before the transition. The turbulent dissipation, $\rho\omega k$, also show similar trends as shown in Figures 4–10(f) following the pattern of the turbulent kinetic energy.

4. DISCUSSION

The present computations clearly show that as Reynolds number increases there is a transition to a flow dominated by the wall shear stress, as discussed by Lathrop *et al.* [6]. At

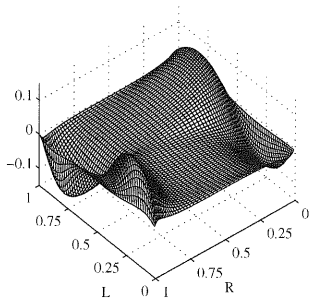

(a) Axial Velocity, $\frac{u_x}{U}$

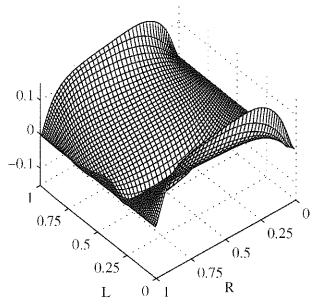

(b) Radial Velocity, $\frac{u_r}{U}$

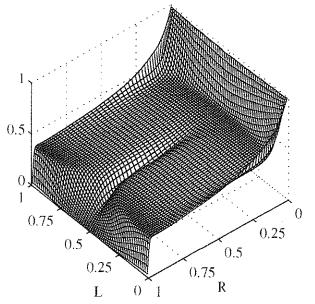

(c) Azimuthal Velocity, $\frac{u_\theta}{U}$

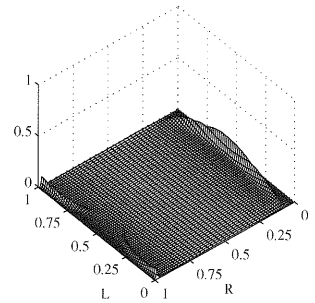

(d) Axial Turbulence Production, $\frac{\nu\mu_T(du_\theta/du_x)^2}{\rho {u_\tau}^4}$

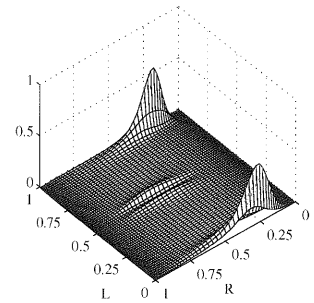

(e) Radial Turbulence Production, $\frac{\nu\mu_T(du_\theta/du_r)^2}{\rho {u_\tau}^4}$

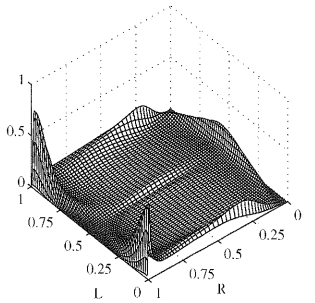

(f) Turbulent Dissipation, $\rho\omega k \cdot \frac{\nu}{u_\tau \rho}$

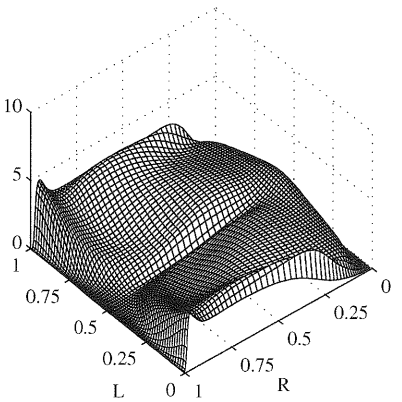

(g) Turbulent Energy, $\frac{k}{{u_\tau}^2}$

Figure 4. Components for square 48 mm case $Re = 8 \times 10^3$.

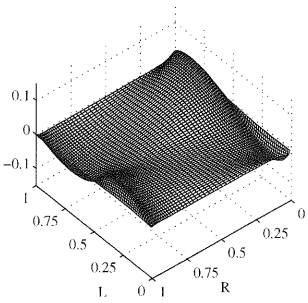

(a) Axial Velocity, $\frac{u_x}{U}$

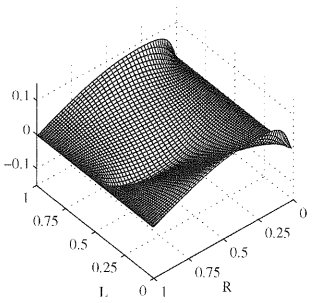

(b) Radial Velocity, $\frac{u_r}{U}$

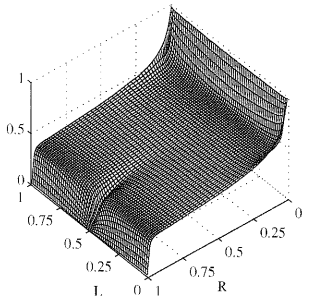

(c) Azimuthal Velocity, $\frac{u_\theta}{U}$

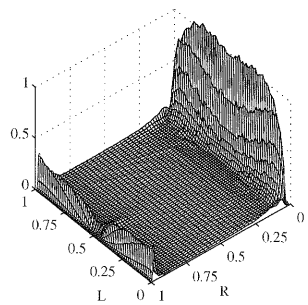

(d) Axial Turbulence Production, $\frac{\nu\mu_T(du_\theta/du_x)^2}{\rho {u_\tau}^4}$

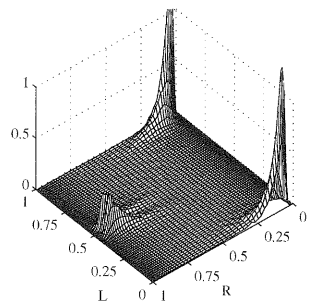

(e) Radial Turbulence Production, $\frac{\nu\mu_T(du_\theta/du_r)^2}{\rho {u_\tau}^4}$

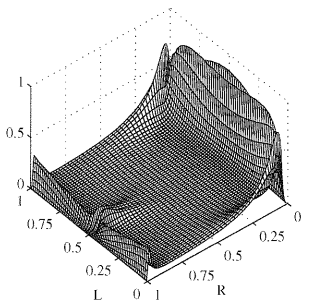

(f) Turbulent Dissipation, $\rho\omega k \cdot \frac{\nu}{u_\tau \rho}$

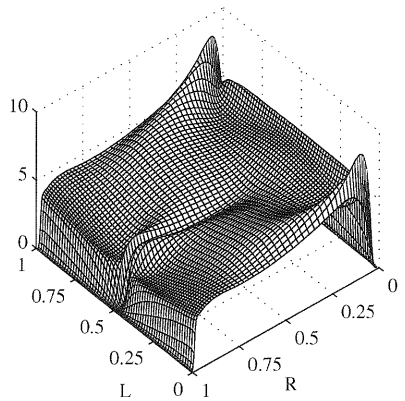

(g) Turbulent Energy, $\frac{k}{{u_\tau}^2}$

Figure 5. Components for square 48 mm case $Re = 2 \times 10^4$.

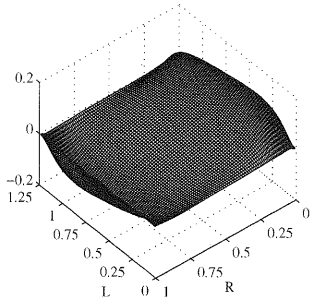

(a) Axial Velocity, $\frac{u_x}{U}$

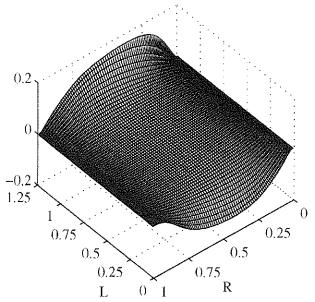

(b) Radial Velocity, $\frac{u_r}{U}$

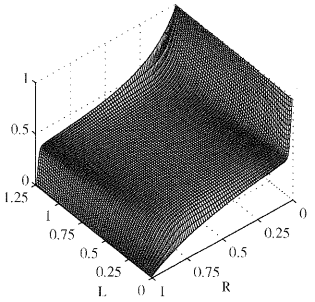

(c) Azimuthal Velocity, $\frac{u_\theta}{U}$

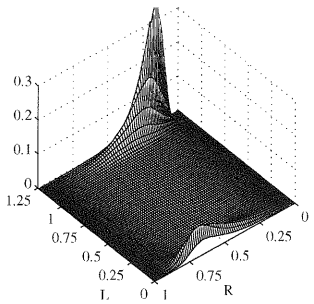

(d) Axial Turbulence Production, $\frac{\nu\mu_T(du_\theta/du_x)^2}{\rho {u_\tau}^4}$

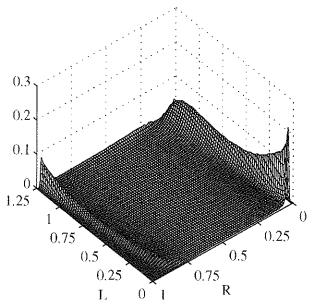

(e) Radial Turbulence Production, $\frac{\nu\mu_T(du_\theta/du_r)^2}{\rho {u_\tau}^4}$

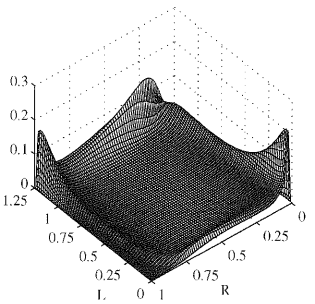

(f) Turbulent Dissipation, $\rho\omega k \cdot \frac{\nu}{u_\tau \rho}$

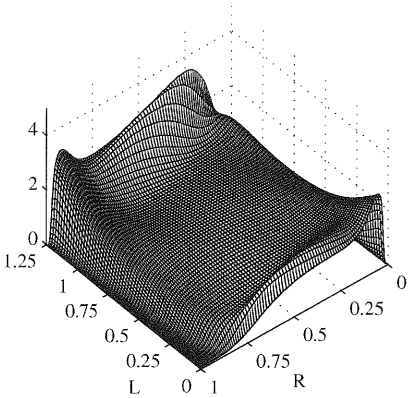

(g) Turbulent Energy, $\frac{k}{{u_\tau}^2}$

Figure 6. Components for 48 mm case $Re = 8 \times 10^3$.

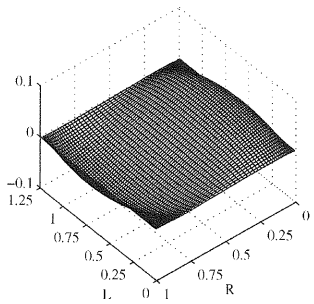

(a) Axial Velocity, $\frac{u_x}{U}$

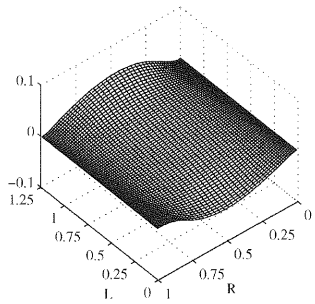

(b) Radial Velocity, $\frac{u_r}{U}$

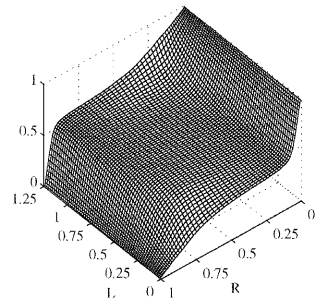

(c) Azimuthal Velocity, $\frac{u_\theta}{U}$

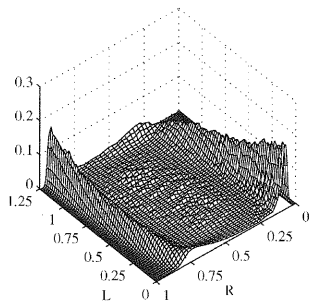

(d) Axial Turbulence Production, $\frac{\nu\mu_T(du_\theta/du_x)^2}{\rho {u_\tau}^4}$

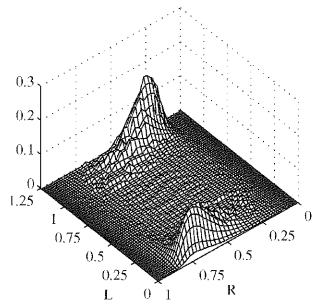

(e) Radial Turbulence Production, $\frac{\nu\mu_T(du_\theta/du_r)^2}{\rho {u_\tau}^4}$

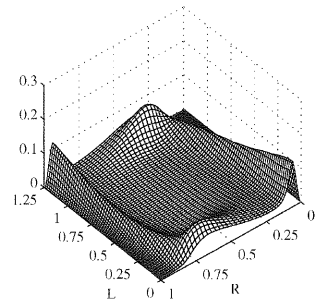

(f) Turbulent Dissipation, $\rho\omega k \cdot \frac{\nu}{u_\tau \rho}$

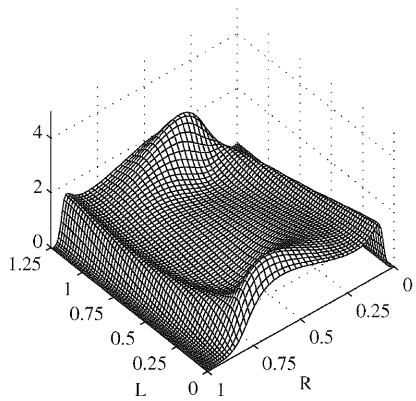

(g) Turbulent Energy, $\frac{k}{{u_\tau}^2}$

Figure 7. Components for 2 mm case $Re = 5 \times 10^3$.

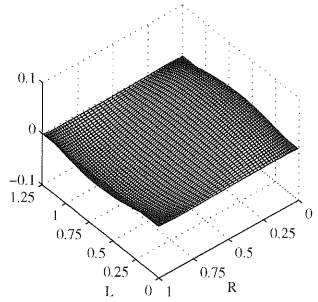

(a) Axial Velocity, $\frac{u_x}{U}$

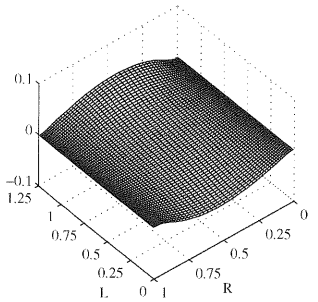

(b) Radial Velocity, $\frac{u_r}{U}$

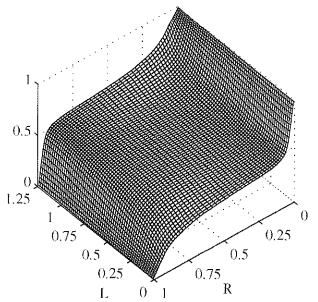

(c) Azimuthal Velocity, $\frac{u_\theta}{U}$

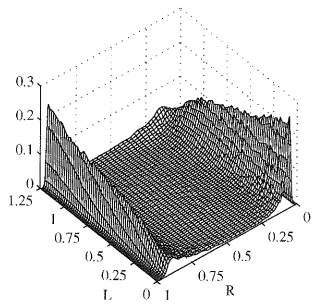

(d) Axial Turbulence Production, $\frac{\nu\mu_T(du_\theta/du_x)^2}{\rho{u_\tau}^4}$

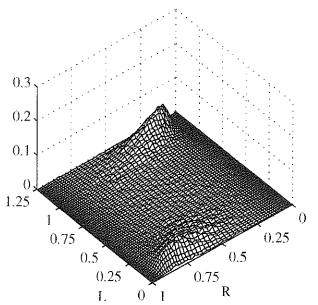

(e) Radial Turbulence Production, $\frac{\nu\mu_T(du_\theta/du_r)^2}{\rho{u_\tau}^4}$

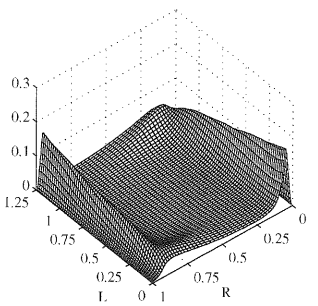

(f) Turbulent Dissipation, $\rho\omega k \cdot \frac{\nu}{u_\tau\rho}$

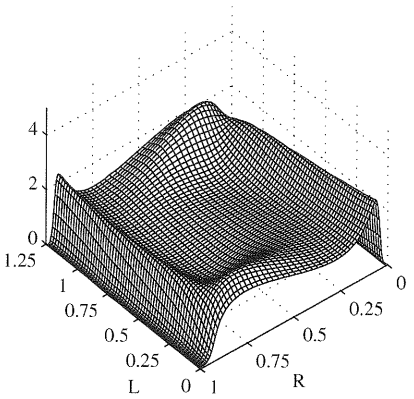

(g) Turbulent Energy, $\frac{k}{{u_\tau}^2}$

Figure 8. Components for 2 mm case $Re = 8 \times 10^3$.

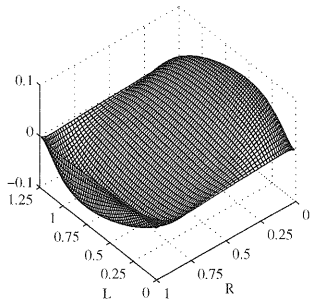

(a) Axial Velocity, $\frac{u_x}{U}$

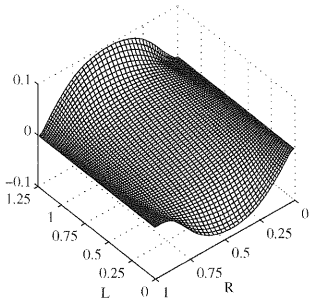

(b) Radial Velocity, $\frac{u_r}{U}$

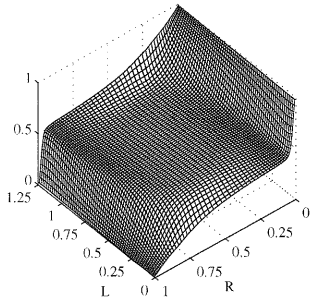

(c) Azimuthal Velocity, $\frac{u_\theta}{U}$

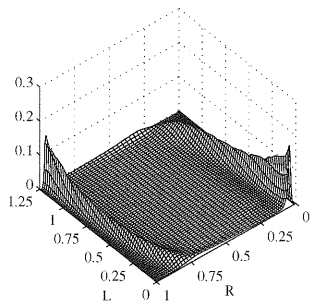

(d) Axial Turbulence Production, $\frac{\nu\mu_T(du_\theta/du_x)^2}{\rho{u_\tau}^4}$

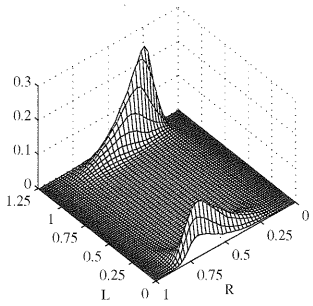

(e) Radial Turbulence Production, $\frac{\nu\mu_T(du_\theta/du_r)^2}{\rho{u_\tau}^4}$

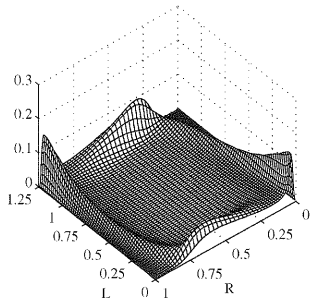

(f) Turbulent Dissipation, $\rho\omega k \cdot \frac{\nu}{u_\tau\rho}$

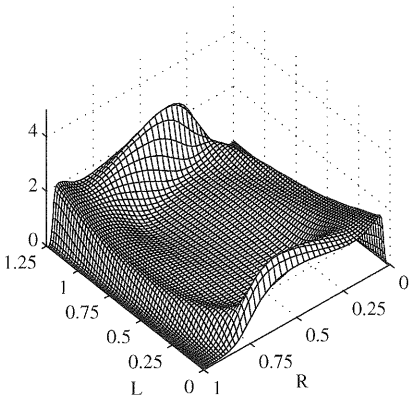

(g) Turbulent Energy, $\frac{k}{{u_\tau}^2}$

Figure 9. Components for 8 mm case $Re = 8 \times 10^3$.

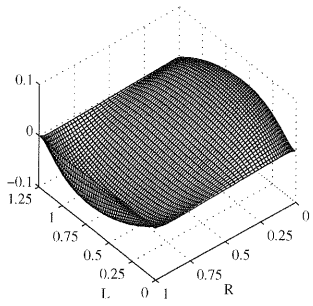

(a) Axial Velocity, $\frac{u_x}{U}$

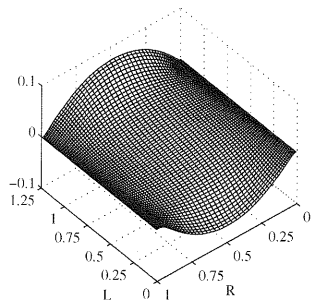

(b) Radial Velocity, $\frac{u_r}{U}$

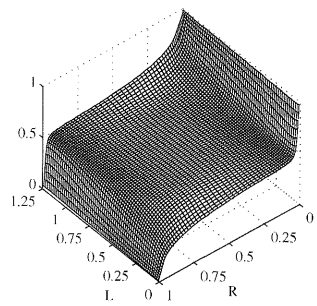

(c) Azimuthal Velocity, $\frac{u_\theta}{U}$

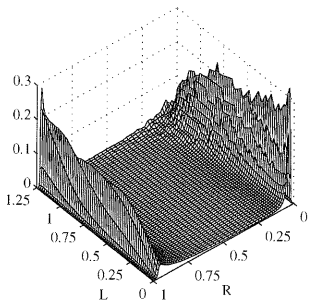

(d) Axial Turbulence Production, $\frac{\nu\mu_T(du_\theta/du_x)^2}{\rho {u_\tau}^4}$

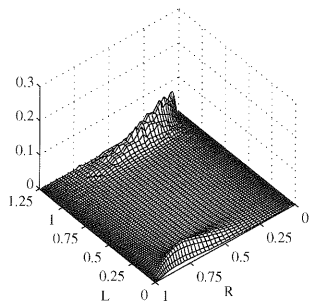

(e) Radial Turbulence Production, $\frac{\nu\mu_T(du_\theta/du_r)^2}{\rho {u_\tau}^4}$

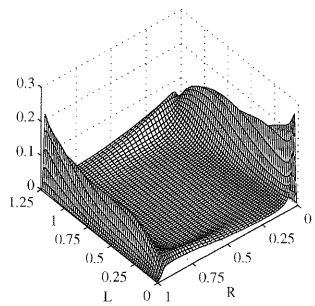

(f) Turbulent Dissipation, $\rho\omega k \cdot \frac{\nu}{u_\tau \rho}$

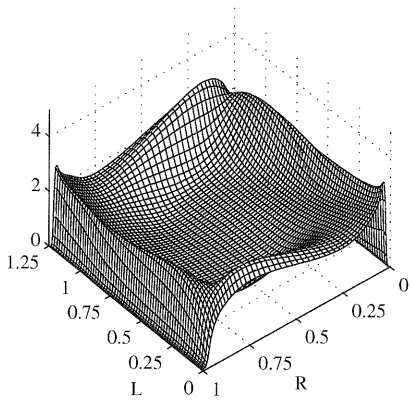

(g) Turbulent Energy, $\frac{k}{{u_\tau}^2}$

Figure 10. Components for 8 mm case $Re = 1.6 \times 10^4$.

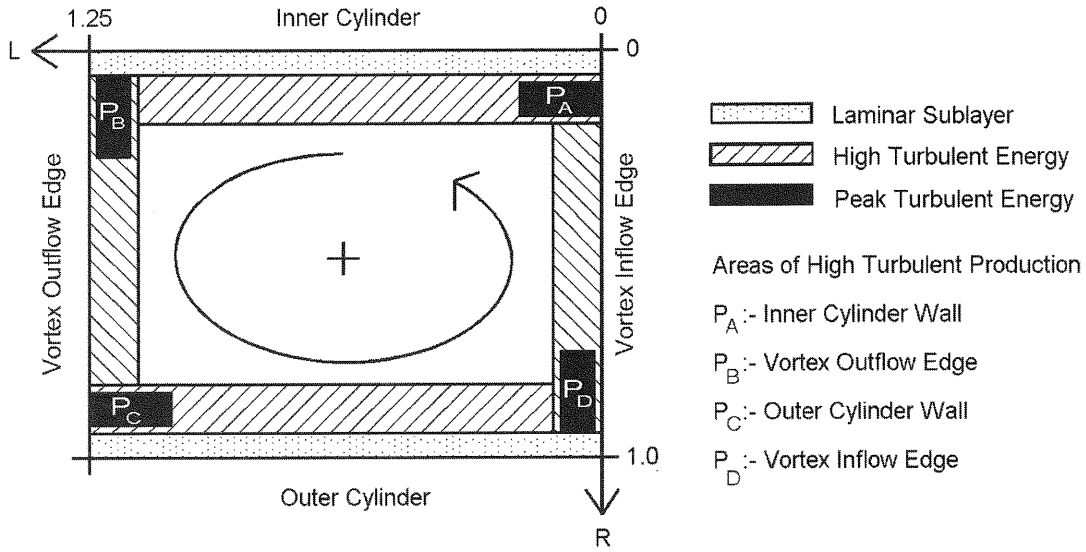

Figure 11. Schematic drawing of a Taylor vortex indicating areas of high turbulent energy.

lower Reynolds numbers turbulence production is dominated by the outflow of the Taylor vortex.

This is represented schematically in Figure 11 where regions P_A and P_C are associated with the turbulent wall shear stress production and P_B and P_C are associated with the vortex inflow and outflow shear stresses, where,

$$P_A < P_B \quad \text{and} \quad P_C < P_D \quad \text{before transition}$$

$$P_A > P_B \quad \text{and} \quad P_C > P_D \quad \text{after transition}$$

For the higher Reynolds number cases turbulence production is dominated by the wall shear stress derivative $(\partial u_\omega/\partial r)^2$ signified by P_A.

The results suggest that the transition to wall dominated turbulent production occurs at a lower Reynolds number for higher radius ratios. This can be demonstrated by comparing Figures 8 and 9. Both these test cases are at the same Reynolds number but the transition has occurred for the 2mm case but not the 8mm case. This is due to the fact that Ta/Ta_c is around 75 per cent lower for the 2mm case. Hence the vortex strength is less, see Figures 8 and 9(a) and (b). This in turn leads to relatively less turbulent production at the vortex outflow and inflow edges, hence the transition occurs at a lower Reynolds number. It is also of interest to note that the non-dimensionalized radial and axial velocity components are higher before the transition.

The problem has also been tested using a low Reynolds number k-ε model [19]. At Reynolds numbers below 10^4 no turbulent energy is produced. For Reynolds numbers between $1 \times 10^4 < Re < 5 \times 10^4$ the solution appears to be unsteady. This is possibly due to the damping function used to implement the low Reynolds number effects as opposed to the adoption of the wall treatment which is applied in the k-ω model.

If the end mirror boundaries are replaced with periodic boundaries an axial flow is developed instead of the Taylor vortices. Also, unsteady disturbances were produced on the surface of the inner cylinder, which may be akin to Görtler vortices but which are not distinguishable in a 2-D flow.

The SimpleC pressure correction algorithm was also compared with the iterative PISO approach. In the latter case the laminar boundary layer produced was larger than expected (approx 40 per cent of the gap width) and consequently, the torques produced were 20 per cent less than predicted by Bilgen and Boulos [9].

5. CONCLUSIONS

A transition in turbulent flow in the Taylor–Couette system with an inner cylinder rotating and a fixed outer cylinder has been identified for a wide range of radius ratios. At relatively low Reynolds numbers turbulent production is dominated by the flow between two adjacent Taylor vortices. A transition occurs as the Reynolds number is increased to a condition where the shear stress of the rotating cylinder becomes the dominant source of turbulent kinetic energy production. It has also been shown that developed turbulent flow can occur for $Ta/Ta_c < 1000$ for small gaps and that the transition occurs earlier for these flows. The results also demonstrate the applicability of the k-ω model to the 2-D simulation of rotating fluids associated with turbulent Taylor vortices.

REFERENCES

1. Hughes AW, Abu-Sharkh SM, Turnock SR. Design and testing of a novel electromagnetic tip driven thruster for underwater vehicles. In *Tenth International Offshore and Polar Engineering Conference (ISOPE)*, Seattle, May 2000.
2. Hughes AW, Turnock SR, Abu-Sharkh SM. CFD modelling of a novel electromagnetic tip driven thruster for underwater vehicles. In *Tenth International Offshore and Polar Engineering Conference (ISOPE)*, Seattle, May 2000.
3. Hughes AW. Investigation of tip-driven thruster and waterjet propulsion systems. PhD Thesis, School of Engineering Sciences, University of Southampton, 2000.
4. Taylor GI. Stability of a viscous liquid contained between two rotating cylinders. *Transitions of the Royal Society of London, A* 1923; **233**:289–343.
5. Koschmieder EL. *Bénard Cells and Taylor Vortices*, 1st edn. Cambridge University Press: Cambridge.
6. Lathrop DP, Fineberg J, Swinney HL. Transition to shear-driven turbulence in Couette–Taylor flow. *Physical Review A* 1992; **46**(10):6390–6405.
7. Wild PM, Djilali N, Vickers GW. Experimental and computational assessment of windage losses in roatating machinery. *Transactions of ASME, Journal of Fluids Engineering* 1996; **118**:116–122.
8. Wilcox DC. *Turbulence Modeling for CFD*, 2nd edn. DCW Industries, 1998.
9. Bilgen E, Boulos E. Functional dependence of torque coefficient of coaxial cylinders on gap width and Reynolds numbers. *Transactions of ASME, Journal of Fluids Engineering* 1973; **95**:122–126.
10. Taylor GI. Fluid friction between rotating cylinders, 1-torque measurements. *Proceedings of the Royal Society of London A* 1936; **157**:546.
11. Donnelly RJ, Simon NJ. An empirical torque relation for supercritical flow between rotating cylinders. *Journal of Fluid Mechanics* 1959; **7**:401.
12. Di Prima RC, Swinney HL. Instabilities and transition in flow between concentric rotating cylinders. In 2nd edn, *Hydrodynamics Instabilities and the Transition to Turbulence*, Swinner HL, Gollub JP (eds). 1981:139–180.
13. Chossat P, Iooss G. *The Couette–Taylor Problem*. Springer: Berlin, 1992.
14. Burkhalter JE, Koschmieder EL. Steady supercritical Taylor vortices after sudden starts. *Physics of Fluids* 1974; **17**(11):1929–1935.
15. Townsend AA. Axisymmetric Couette flow at large Taylor numbers. *Journal of Fluid Mechanics* 1984; **144**: 329–362.

16. Parker J, Merati P. An investigation of turbulent Taylor–Couette flow using laser doppler velocimetry in a refractive index matched facility. *Transactions of ASME, Journal of Fluids Engineering* 1996; **118**:810–818.
17. Launder BE, Spalding DB. The numerical computations of turbulent flow. *Computational Methods of Applied Mechanical Engineering* 1974; **13**:269–289.
18. Yakhot V, Orszag S. Renormalization group analysis of turbulence. *Journal of Scientific Computing* 1986; **1**(1):3–57.
19. Launder BE, Reece GJ, Rodi W. Progress in the development of a Reynolds-stress turbulent closure. *Journal of Fluid Mechanics* 1975; **63**:537–566.
20. Chandrasekhar S. *Hydrodynamic and Hydromagnetic Stability*. Clarendon Press: Oxford, 1961.
21. AEA Technology plc. *CFX-4.3 Solver*, 1997.

